Wavelength Tunable Fiber Lens Based on Multimode Interference

Waleed S. Mohammed, Alok Mehta, and Eric G. Johnson

Abstract—A new concept for a fiber-based wavelength-tunable condensing lens is theoretically and experimentally investigated in terms of its ability to shift the longitudinal focus position as a function of wavelength. By exploiting multimode interference effects with reimaging theory, a compact and robust device, completely contained within a standard FC connector, can be constructed by simply splicing a single-mode fiber (SMF) to a finite length section of multimode fiber (MMF). This paper summarizes the theoretical and experimental results of such a device, with additional results for wavelength sensitivity.

Index Terms—Optical beam focusing, optical fiber devices, optical fiber interference, optical position measurement.

I. INTRODUCTION

MULTIMODE interference effects combined with single reimaging conditions [1] provide the basis for the operation of our device. In the past, multimode interference theory has been utilized in the design and fabrication of devices such as modulators [2] and Mach–Zehnder switches [3]. For an input field centered symmetrically around the optical axis incident on the input facet of a multimode fiber (MMF), multimode interference effects result in periodic longitudinal locations within the fiber where the source field is duplicated. Through characterization of this reimaging effect in a MMF, it is possible to design and fabricate a device that provides a mechanism to overcome the natural tendency for the light to diverge when exiting the fiber. Traditionally, when fiber-based devices are designed and fabricated, it is assumed that collimating optics have been incorporated to combat the natural divergence of the exiting beam [4]. In fact, some approaches actually involve fabricating lenses on the ends of the fiber [5]. The device we present essentially performs a lensing operation on the input field incident to the MMF, condensing the light to wavelength dependent longitudinal locations outside the fiber. By analogy to the traditional lens, we will call these locations outside the MMF where the field condenses focal planes using our virtual lens model. These locations and associated spot sizes are a function of the core diameter of the MMF, the material properties of the fiber, and the wavelength of the source. We present a method to theoretically predict the shift of the focal plane as a function of wavelength in comparison to experimentally observed behavior and results obtained through FD-BPM simulations. These FD-BPM simulations are also used to verify the validity of the model we present for the

determination of the beam spot size observed at the wavelength dependent locations where the output beam is condensed.

A. Theory

The basis for this paper lies in the concept of reimaging based on the multimode interference effect associated with multimode waveguides as was done for the case of a planar waveguide in [1]. The reimaging distance is where the input source is replicated in both amplitude and phase. In contrast to the planar waveguide approach, a reimaging condition is established for a circular multimode waveguide. Moreover, fractional planes are defined where light appears to be concentrated [see Fig. 1(a) and (b)]. The specific planes where field concentration and reimaging occur are determined through use of analytical approximations that are derived on the premise that the input light source is provided by a single-mode fiber (SMF) fusion spliced to a section of MMF.

B. SMF to MMF Coupling

In order to determine the longitudinally located reimaging locations inside a MMF fiber, with an input field provided from a SMF fusion spliced directly to the MMF, it is necessary to first determine which modes are excited in the MMF based on the SMF source. This may be derived by the coupling efficiency associated with the propagating modes within the MMF. Using the linearly polarized mode approximation, the input field provided from the SMF $\overline{E}_s(r)$ can be approximated as a Gaussian beam.

$$\overline{E}_s(r) = e^{-(r/\varpi)^2} e^{-i\beta_o z} \hat{x} \tag{1}$$

where β_o is the longitudinal propagation constant for the SMF guided mode LP_{01}. The half-width at half-maximum (HWHM) spot size ϖ of the Gaussian beam can be determined empirically [8] based on the radius of the SMF, a_o, and the V-number, $V = (2\pi a_o/\lambda)\sqrt{n_{core}^2 - n_{clad}^2}$, where n_{core} and n_{clad} are the core and cladding refractive indexes, respectively

$$\varpi = \frac{a_o}{\sqrt{\ln 2}} \left(0.65 + 1.619\,V^{-1.5} + 2.879\,V^{-6} \right). \tag{2}$$

This input field excites a specific number of guided modes inside the MMF. These modes, together with the radiating modes, form an orthogonal set [11]. Neglecting the radiating modes, the field distribution at any point in the MMF can be written as a series expansion of the guided modes as depicted in (3)

$$\bar{E}(r, \theta, z) = \sum_{\mu=-M}^{M} \sum_{v=1}^{N} \bar{\psi}_{v,\mu}(r, \theta, z). \tag{3}$$
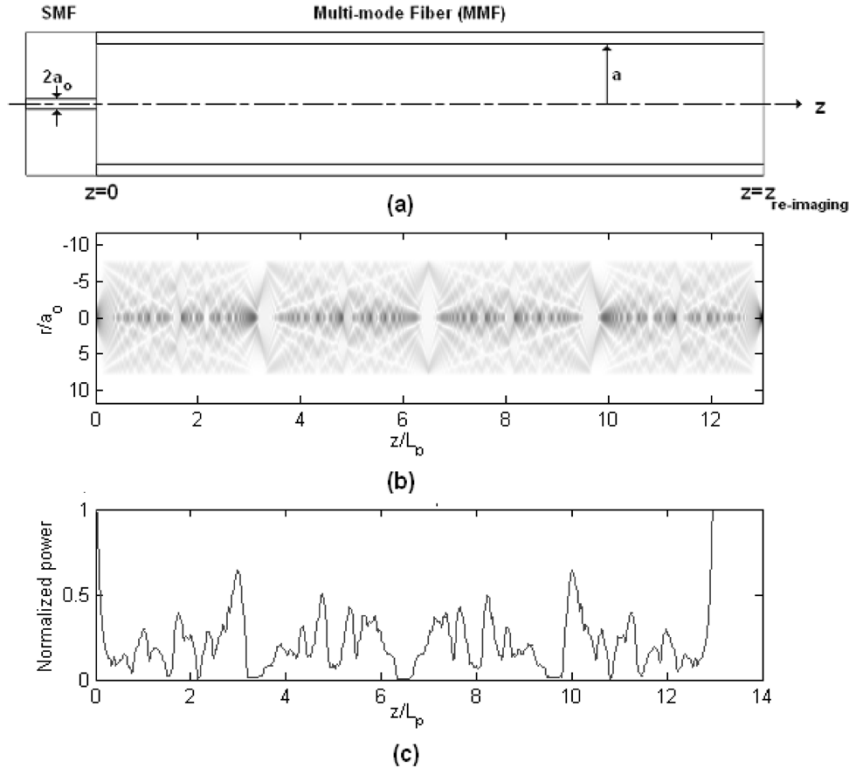
Fig. 1.   (a) Geometry of the device: SMF fusion spliced to a MMF. (b) Amplitude distribution of the light inside the MMF for the fibers parameters cited in Table I. (c) Power, normalized to the input power, displayed across an area equal to the SMF core along the optical axis of the MMF.

In (3) the suffixes v and μ are the indexes for the guided radial and azimuthal components, respectively. N and $2M + 1$ are the total number of radial and azimuthal modes, respectively. $\bar{\psi}_{v,\mu}(r,\theta,z)$ represents the complex field vector of the guided mode. Applying the separation of variables and solving Maxwell equations inside the MMF for linearly polarized modes, $\bar{\psi}_{v,\mu}(r,\theta,z)$ can be written as follows [7]:

$$\bar{\psi}_{v,\mu}(r,\theta,z) = \begin{cases} c_{v,\mu} J_\mu \left(u_{v,\mu}\frac{r}{a}\right)\cos(\mu\theta)e^{-i\beta_{v,\mu}z}\hat{x} & r \le a \\ d_{v,\mu} K_\mu \left(w_{v,\mu}\frac{r}{a}\right)\cos(\mu\theta)e^{-i\beta_{v,\mu}z}\hat{x} & r > a \end{cases} \tag{4}$$

where $u_{v,\mu}$, $w_{v,\mu}$, $\beta_{v,\mu}$, and a are the normalized transverse propagation constant inside the core, in the cladding, longitudinal propagation constant for this mode and the radius of the MMF, respectively. The normalized transverse wavenumber $u_{v,\mu}$ and $w_{v,\mu}$ are defined as $u_{v,\mu} = a\sqrt{k_o^2 n_{\text{core}}^2 - \beta_{v,\mu}^2}$ and $w_{v,\mu} = a\sqrt{\beta_{v,\mu}^2 - k_o^2 n_{\text{clad}}^2}$, n_{core} and n_{clad} are the core and cladding refractive indexes, respectively, and k_o is the wavenumber in free space. $c_{v,\mu}$ and $d_{v,\mu}$ are field excitation constants related through the following relation: $d_{v,\mu} = (J_\mu(u_{v,\mu})/K_\mu(w_{v,\mu}))c_{v,\mu}$. Thus, (4) can be incorporated into (3) to represent the radial and azimuthal modes within the MMF. At $z = 0$, the left-hand side (LHS) of (3) should equal the input field $E_s(r)$ as shown in the geometry of Fig. 1(a).

At the $z = 0$ position, the field expressions describing the modes present within the MMF represent a projection of the input field onto an orthogonal set of the transverse field components of the guided modes. Thus, the expansion coefficients, $c_{v,\mu}$ and $d_{v,\mu}$, are the field excitation coefficients. Moreover, re-calling that the representation of the input field in (1) does not contain any azimuthal components, the field distribution inside the MMF also lacks any azimuthal components. This forces the excitation coefficient to vanish for values of $\mu \ne 0$. This constraint simplifies the representation for the field within the MMF into a sum of radial modes. Thus, the modes that are excited inside the MMF are purely radial modes and expressed as follows

$$\overline{E}_s(r,0) = \begin{cases} \sum_{v=1}^{N} c_{v,0} J_0 \left(u_{v,0}\frac{r}{a}\right)\hat{x} & r \le a \\ \sum_{v=1}^{N} d_{v,0} K_0 \left(w_{v,0}\frac{r}{a}\right)\hat{x} & r > a. \end{cases} \tag{5}$$

For simplicity we will omit the suffix for the azimuthal modes and write the excitation coefficients, the normalized traverse propagation constant and the longitudinal propagation constant as c_v, d_v, u_v, and β_v, respectively. To calculate the field excitation coefficients, we will use the well know figure of merit; the power coupling coefficient η_v. The power coupling coefficient determines the amount of the input field power that couples to each specific mode in the MMF. In terms of an overlap integral in cylindrical coordinates η_v can be determined using the following equation:

$$\eta_v = \frac{\left|\int_0^\infty E_s(r)E_v(r)r\,dr\right|^2}{\int_0^\infty |E_s(r)|^2 r\,dr \int_0^\infty |E_v(r)|^2 r\,dr}. \tag{6}$$

$E_v(r)$ represents the field distribution of the vth guided radial mode. Using the fact that the input field is much smaller than the actual core diameter of the MMF itself, we can neglect the extension of the mode field in the cladding region in the nominator

of (6). Using this assumption, the field excitation coefficient, c_v, can be related to the power coupling efficiency, η_v, through $c_v = \sqrt{\eta_v}$ as the integration in the numerator in (6) is the cross correlation between the input and the core fields. In this case the overlap integral can be written as shown in (7) at the bottom of the page. Using Hankel Transform properties, an analytical solution can be deduced as a function of the guided modes and the terms dependant on the physical parameters of the fibers used (see (8) at the bottom of the page). From the asymptotic formulation for the roots of the zeroth-order Bessel function as done in [11], the normalized transverse wavenumbers can be written as

$$u_v = \left(2v - \frac{1}{2}\right)\frac{\pi}{2} \tag{9}$$

$$w_v = \sqrt{V^2 - \left(\left(2v - \frac{1}{2}\right)\frac{\pi}{2}\right)^2} \tag{10}$$

where V is the V–number of the MMF defined as $V^2 = u_v^2 + w_v^2$. Thus, (8) can be modified into the following form (see (11) at the bottom of the page). Using the equation above, the power coupling coefficient is calculated for all the allowed radial modes inside two different MMF that have the same material properties as in Table I, but two different radii: 52.5 and 92.5 μm. The results for these two scenarios are depicted in Fig. 2. The most pronounced feature in the graph is the presence of a peak coupling efficiency associated with a specific mode number. This feature is the key for predicting the reimaging and the fractional planes where light is concentrated as will be presented in Section I-C.

C. Reimaging Conditions

We present an analytical formulation of the location of the reimaging and the fractional planes where light is concentrated

TABLE I
OPTICAL FIBER CHARACTERISTICS OF FABRICATED DEVICE AND
PARAMETERS USED FOR MODELING

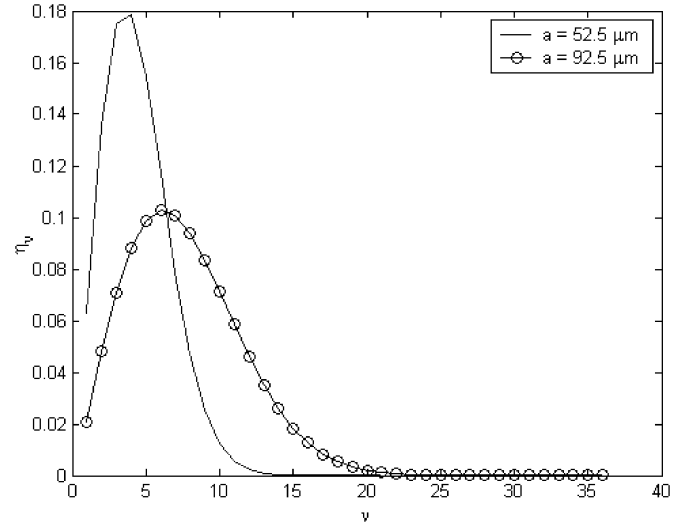| FIBER DESCRIPTION	CORE RADIUS (μm)	CLADDING RADIUS (μm)	CORE REFRACTIVE INDEX
SMF-28	4.5	62.5	1.4505
Step Index MMF	52.5	62.5	1.479

Fig. 2. Coupling efficiency as function of mode number for MMF core radii of 52.5 and 92.5 μm, respectively, using a SMF launch.

using the fact that the power coupling efficiency is maximum for a specific mode number. In order to determine which radial guided mode has the highest coupling efficiency associated with

$$\eta_v = \frac{\left|\int_0^\infty \exp\left[-\left(\frac{r^2}{\omega^2}\right)\right] J_0\left(\frac{u_v r}{a}\right) r\, dr\right|^2}{\int_0^\infty \exp\left[-\left(\frac{2r^2}{\omega^2}\right)\right] r\, dr \left[\int_0^a J_0\left(u_v \frac{r}{a}\right)^2 r\, dr + \left(\frac{J_0(u_v)}{K_0(w_v)}\right)^2 \int_a^\infty K_0\left(w_v \frac{r}{a}\right)^2 r\, dr\right]}. \tag{7}$$

$$\eta_v = \frac{2\left(\frac{\omega}{a}\right)^2 \exp\left[-\left(\frac{\omega^2}{a}\right)\left(\frac{u_v^2}{2}\right)\right]}{J_0^2(u_v) + J_1^2(u_v) + \left(\frac{J_0(u_v)}{K_0(w_v)}\right)^2 (K_1^2(w_v) - K_0^2(w_v))}. \tag{8}$$

$$\eta_v = \frac{2\left(\frac{\omega}{a}\right)^2 \exp\left[-\frac{1}{2}\left(\frac{\omega^2}{a}\right)\left(\left(2v - \frac{1}{2}\right)\frac{\pi}{2}\right)^2\right]}{J_0^2\left(\left(2v - \frac{1}{2}\right)\frac{\pi}{2}\right) + J_1^2\left(\left(2v - \frac{1}{2}\right)\frac{\pi}{2}\right) + \left(\frac{K_1^2\left(\sqrt{V^2 - \left(\left(2v - \frac{1}{2}\right)\frac{\pi}{2}\right)^2}\right)}{K_0^2\left(\sqrt{V^2 - \left(\left(2v - \frac{1}{2}\right)\frac{\pi}{2}\right)^2}\right)} - 1\right) J_0^2\left(\left(2v - \frac{1}{2}\right)\frac{\pi}{2}\right)}. \tag{11}$$

it, it is necessary to look at the derivative of the coupling coefficient with respect to the mode number as shown in Appendix A (see (12) at the bottom of the page). The zeros for (12) are determined using a combination of bisection, secant, and inverse quadratic interpolation methods. These solutions to (12) result in the value of $v = v_p$ that maximizes the coupling coefficient. This mode is, in general, the most dominant radial mode in the MMF. In order for light within the MMF to be concentrated to an on axis location, it is necessary for the phase difference between the peak mode v_p and the adjacent mode to equal an integer multiple of 2π. Moreover, we predict that the reimaging condition should be a special case of this criteria, or more specifically, a specific integer multiple of the distance characteristic of a location where field condensation occurs.

Under the asymptotic formulation given in [12], the difference in the longitudinal propagation constants between two radial modes v_1 and v_2 can be expressed as follows where u_{v_1} and u_{v_2} are provided in (9) for the asymptotic formulation for the roots of the zeroth-order Bessel function

$$(\beta_{v1} - \beta_{v2}) = \frac{u_{v2}^2 - u_{v1}^2}{2k_o a^2 n_{\text{core}}}. \tag{13}$$

Considering the two modes v_p and $v_p - 1$, the phase difference between these two modes can thus be expressed as in

$$(\beta_{v_p - 1} - \beta_{v_p}) z = \frac{\pi^2 (4v_p - 3)}{4k_o a^2 n_{\text{core}}} z. \tag{14}$$

At the following longitudinal location inside the MMF along the optical axis z_{m}

$$z_{\text{m}} = \frac{8ka^2 n_{\text{core}}}{\pi(4v_p - 3)} m = L_p m, \quad m = 1, 2, 3, \ldots$$
$$L_p = \frac{8ka^2 n_{\text{core}}}{\pi(4v_p - 3)} \tag{15}$$

the phase difference becomes an integer multiple of 2π. L_p corresponds to the location where the phase difference between the two modes equals 2π. Recalling Fig. 1(b), the upper part shows the Intensity distribution across the MMF calculated using (3) for the fiber properties mentioned in Table I. The lower part of the figure shows the average intensity distribution around the central region normalized to the input intensity. In this portion of this graph, we see pronounced maxima at $m = 0, 1, 3, 10, 12,$ and 13. Besides these locations, there are several maxima approximately corresponding to the values of $m = 2, 5, 8,$ and 11. This serves to justify the statement made previously that there are several locations, z_{m}, corresponding to local maxima along the axis of the MMF where field condensation occurs. Although these locations might not be explicit reimaging locations of the input field, they do correspond to locations where condensing of power along the optical axis occurs.

The explicit reimaging location where the source input field is duplicated is derived from the representation of the field given in (3). Looking at the complex field vector contained in this formulation, the phase term can be manipulated by factoring out the phase term characteristic of the radial mode that has a maximum coupling associated to it, $e^{-i\beta_{v_p} z}$. By doing so, the reimaging distance can be determined by looking at the resulting phase difference term, $(\beta_v - \beta_{vp})z$. The reimaging distance is defined as the distance, $z_{re\text{-imaging}}$, that corresponds to when this phase difference between these two guided radial modes equaling an integer multiple of 2π. Therefore, under the asymptotic assumption for the lateral propagation constants, the reimaging distance can be calculated as follows by formulating an expression for the phase difference between the vth and v_p modes as done in (14)

$$(\beta_v - \beta_{v_p}) z = \frac{\pi^2 \left[2 \left(v^2 - v_p^2 \right) + (v_p - v) \right]}{4n_{\text{core}} ka^2} z$$
$$= 2\pi p, \quad p : \text{Integer.} \tag{16}$$

Thus, the distance that the two modes must propagate to satisfy the reimaging conditions can be expressed as

$$z_{re\text{-imaging}} = \frac{8n_{\text{core}} ka^2}{\pi}. \tag{17}$$

In comparing (15)–(17), we can see that $z_{re\text{-imaging}}$ is indeed an integer multiple of L_p when expressed in the following manner

$$z_{re\text{-imaging}} = (4v_p - 3)L_p. \tag{18}$$

Having determined the specific planes inside the MMF where field condensation and reimaging occurs, it is now necessary to present the use of this device to condense the light exiting the end facet of the MMF. In Section I-D, we will demonstrate a novel and simple technique that uses the phenomenon discussed above to create a fiber-based wavelength tunable condensing lens.

D. Fiber-Based Wavelength Tunable Condensing Lens

To force light exiting the MMF to converge toward the optical axis, the actual length of the MMF, L_{MMF}, has to be slightly less than the length specified by (15) for a chosen integer value of m. By doing so, it is possible to determine the locations along the optical axis where field condensation will occur. Phase difference relations can be used to determine these locations by taking into account the propagation within the MMF and the propagation in free space to the locations outside the MMF where the field condensation is observed. The following equation is derived from this phase difference relation keeping in mind that the propagation constants are wavelength dependent

$$z_{\text{out}} = \frac{2\pi m - L_{\text{MMF}} (\beta_{vp-1} - \beta_{vp})}{\beta_{\text{out},vp-1} - \beta_{\text{out},vp}}. \tag{19}$$

From continuity of the tangential component of the wave vector, the associated longitudinal propagation constant of a particular

$$\frac{\partial \eta_v}{\partial v} = \frac{2\pi \left((2v - \frac{1}{2})\frac{\pi}{2} \right) \left(\frac{\omega}{a} \right)^2 \exp \left[-\frac{1}{2} \left(\frac{\omega^2}{a} \right) \left((2v - \frac{1}{2})\frac{\pi}{2} \right)^2 \right] D_v - \left(\frac{\omega}{a} \right)^2 \exp \left[-\frac{1}{2} \left(\frac{\omega^2}{a} \right) \left((2v - \frac{1}{2})\frac{\pi}{2} \right)^2 \right] D_v'}{D_v^2}$$
$$= 0. \tag{12}$$

mode after exiting the MMF can be determined using the formula below in terms of the longitudinal propagation constant inside the MMF

$$\beta_{\text{out},v} = \sqrt{k_o^2 \left(1 - n_{\text{core}}^2\right) + \beta_v^2}. \tag{20}$$

In formulating (16), the phase term associated with the mode that has a maximum coupling was factored out of the field representation in (3) resulting in a particular phase difference term. In order to determined a first-order formulation for (19), the same phase term factoring approach can be adopted, only for approximation purposes the phase term associated with the fundamental mode β_1 is factored out. In doing so, the same asymptotic approximations made previously can be applied to the $(\beta_1 - \beta_v)$ term contained within the phase difference expression for the field as done in (16). β_v can isolated from this relationship and substituted back into (20). Thus, the longitudinal propagation constant of a particular mode after exiting the MMF into free-space can be formulated as shown in (21) at the bottom of the page. Assuming that the fundamental longitudinal propagation constant β_1 can be approximated as $(k_o n_{\text{core}})$ and that the last squared term in (21) is much smaller than the other terms under the square root, this equation can be simplified as follows:

$$\beta_{\text{out},v} = k_o \sqrt{1 - \frac{2n_{\text{core}}\left(2v + 1\right)\left(v - 1\right)2\pi}{z_{re\text{-imaging}}}}$$
$$\cong k_o - \frac{n_{\text{core}}\left(2v + 1\right)\left(v - 1\right)2\pi}{z_{re\text{-imaging}}}. \tag{22}$$

This approximate formulation for the longitudinal propagation constants outside the MMF can be used to form the expression for the $\beta_{\text{out},vp-1} - \beta_{\text{out},vp}$ term included in (18). Along with the expression for $\beta_{vp-1} - \beta_{vp}$ in (14), (19) can be manipulated into the following equation for the locations along the optical axis where field condensation of the light exiting the MMF occurs

$$z_{\text{out}} = \frac{2\pi m - L_{\text{MMF}}\left(\frac{(4v_p - 3)2\pi}{z_{re\text{-imaging}}(\lambda)}\right)}{\frac{n_{\text{core}}(4v_p - 3)\pi}{z_{re\text{-imaging}}(\lambda)}}. \tag{23}$$

Using the relation defined for L_p in (15), the above equation can be rewritten into a more compact form in terms of L_p, the actual length of the MMF used, and the core refractive index

$$z_{\text{out}} = \frac{mL_p - L_{\text{MMF}}}{n_{\text{core}}}. \tag{24}$$

In terms of the fiber parameters and the wavelength, (24) can be written as follows:

$$z_{\text{out}} = m\frac{16a^2}{(4v_p - 3)\lambda} - \frac{L_{\text{MMF}}}{n_{\text{core}}}. \tag{25}$$
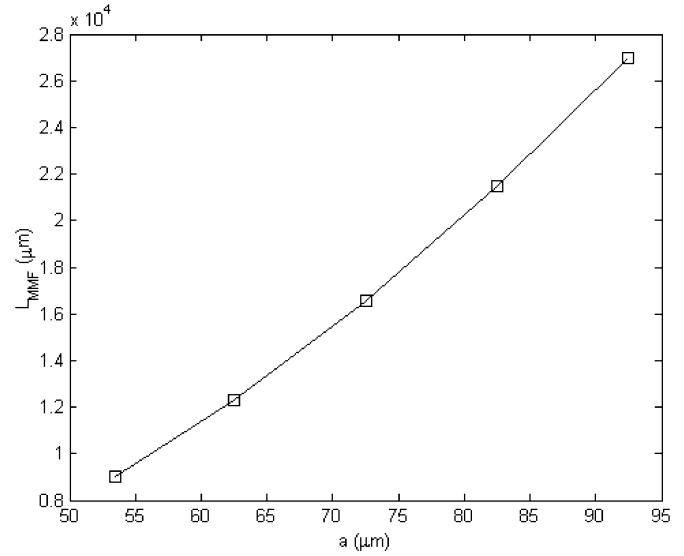

Fig. 3. Change of L_{MMF} versus the MMF radius a. L_{MMF} is considered to be 0.95 of the reimaging distance inside the MMF.

It is important to look at how z_{out} changes when certain system parameters are varied. In particular, it is clear that this output distance has an inherent wavelength dependence. Using the formulation above, the derivative is expressed in (26) demonstrating that z_{out} is approximately constant with respect to the varying wavelength

$$\frac{\partial z_{\text{out}}}{\partial \lambda} = -m\frac{16a^2}{(4v_p - 3)\lambda_o^2}. \tag{26}$$

Another influencing system parameter is the radius of the MMF, a, because the peak mode index v_p, and L_{MMF} depend strongly on the MMF radius. For a specific wavelength λ_o, z_{out} changes considerably when the MMF radius is varied as demonstrated in the following equation

$$\frac{\partial z_{\text{out}}}{\partial a} = -m\frac{32a}{(4v_p - 3)\lambda_o} + m\frac{64a^2}{(4v_p - 3)^2\lambda_o}\frac{\partial v_p}{\partial a}$$
$$- \frac{1}{n_{\text{core}}}\frac{\partial L_{\text{MMF}}}{\partial a}. \tag{27}$$

As the radius of the MMF changes, v_p changes according to solutions of (12). That changes the location of the working maximum, and thus the proper MMF length, L_{MMF}. Using the fiber material parameters in Table I, the change of L_{MMF} as a function of the core radius is depicted in Fig. 3. L_{MMF} is assumed to be 0.95 of the length corresponding to the peak at $(v_p - 1)L_p$.

Having determined the locations outside the MMF where field condensation will occur, in order to estimate the spot size at the focal plane, we need to calculate the intensity distribution outside the MMF. The series expansion in (3) can be used with a modification in the phase term to compensate for the free space propagation. In addition, we can neglect the field expansion in

$$\beta_{\text{out},v} = \sqrt{k^2 - n_{\text{core}}^2 k_o^2 + \beta_1^2 - \frac{2\beta_1\left(2v + 1\right)\left(v - 1\right)2\pi}{z_{re\text{-imaging}}} + \left(\frac{\left(2v + 1\right)\left(v - 1\right)2\pi}{z_{re\text{-imaging}}}\right)^2}. \tag{21}$$
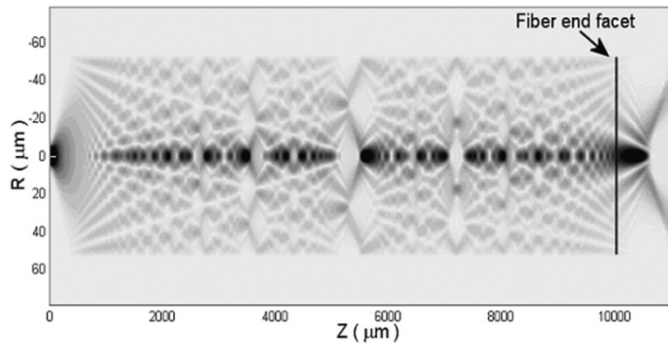
Fig. 4. Calculation of intensity inside MMF ($\lambda = 1.55\ \mu$m) using (5) and (25) for the field inside and outside the MMF. The MMF is polished slightly less than 10 mm (corresponds to $3L_p$). [SMF of 4.5 μm core radius and MMF core radius of 52.5 μm].

Fig. 5. Device connectorized in FC connector and $20 \times$ microscope image of end facet of MMF quality.

the cladding region as most of the power is concentrated in the central region. Thus, the output field can be written as

$$E_{\text{out}}(r, L_{\text{MMF}} + z_{\text{out}})$$
$$= \sum_{v=1}^{N} \sqrt{\eta_v} J_0\left(u_v \frac{r}{a}\right) e^{-i(\beta_v L_{\text{MMF}} + \beta_{\text{out},v} z_{\text{out}})} \quad (28)$$

where β_{out},v is the longitudinal propagation constant for the vth-order mode in air as defined in (22).

E. Results

The tunable fiber optic lens described here is unique with respect to the relative simplicity in fabrication and the ability to significantly change the focal length. It consists of a MMF (Thor Labs AFS105/125) fusion spliced onto a SMF (Corning SMF-28) attached to a tunable laser source via an 80/20 splitter, which allows for detection of any returning signal. Agilent 81635A InGaAs power sensor and 81 640A tunable laser modules were used in conjunction with the 8164 A Lightwave measurement system to make the measurements presented in this paper.

For the fiber parameters cited in Table I, the mode associated with maximum coupling is $v_p = 4$. This can be observed looking at Fig. 2 which shows the relationship between the coupling efficiency and the mode number for MMF core radii of 52.5 and 92.5 μm, respectively. Using these parameters at a wavelength of 1.55 μm results in $L_p = 3.2369$ mm. From (18), the reimaging location is found to be $z_{re\text{-imaging}} = 13L_p = 42.08$ mm. Using these values, Fig. 1(b) is constructed in order to represent the intensity distribution along the axis of the multimode fiber with the length in the z-direction normalized to L_p. As aforementioned, the most significant feature is the presence of very distinguish maxima at locations such as $3L_p$, and $10L_p$. The length of the MMF spliced onto the SMF can be chosen with respect to these distinguished maxima observed inside the MMF. By cleaving the MMF at a length slightly less than the length specified at any one of these locations, the light exiting the fiber converges to an on-axis location in the air outside the fiber as depicted in Fig. 4. In this case, the fiber end facet is located at a longitudinal location that corresponds to a length slightly less than that defined for the $m = 3$ case in (15). If a
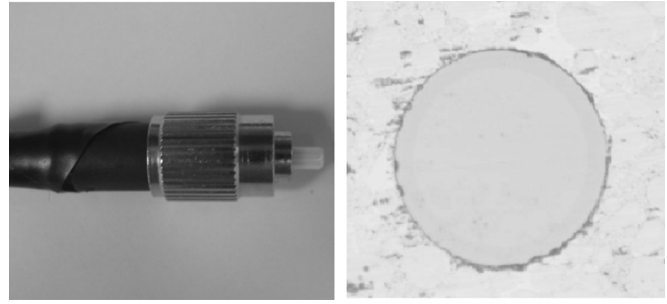
mirror is placed at this same plane, the coupling of the light reflected back through the fiber would be a maximum compared to any other location in the near vicinity which indicates the location of the focal plane. Thus, the shift in the focal plane can be experimentally measured by detecting the power reflected from a mirror placed in front of the end facet of the MMF while sweeping the wavelength. To verify the validity of choosing the a length of MMF less than the $m = 3$ case, a scalar cylindrically symmetric FD-BPM simulation is done for the SMF and step index MMF using the parameters depicted in Table I. Fig. 4 shows specifically the field convergence at longitudinal on axis locations after exiting the end facet of the MMF.

In order to accurately compare experimental and theoretical results, the length of the MMF fusion spliced onto the SMF must be accurately known. The process used to fabricate this device inherently provides this information and a procedure to repeatedly cleave the same length of MMF onto the SMF each time a device is fabricated. Using the scale on the fiber cleaver, a MMF splice length of 21 mm was produced to be fusion spliced to the SMF. Once this was done, a cleave is made 11 mm from the end facet of the MMF, leaving a length less than 10 mm long MMF spliced to the SMF. This length is conveniently slightly less than the $m = 3$ case using the formulation of (15). The actual length of the MMF can be more closely determined using a microscope equipped with a CCD camera. Once the fusion splice interface is found, the calibrated camera software to observe microscope images can be used to provide the distance from this interface to the end facet of the MMF. The bare fiber device was then appropriately connectorized into an FC ferrule with a stereo microscope used to verify that the MMF only barely protruded through the end facet of the FC ferrule. A 0.5 μm polishing disk and colloidal slurry were then used to hand polish the end facet of the MMF until the surface was of optical quality as depicted in Fig. 5.

The SMF and step index MMF used have parameters defined in Table I. As done in [9], sweeping the wavelength of the source into the SMF and observing the reflected power that results for mirror placement at specific longitudinal displacements from the end facet of the MMF, the most notable feature for each waveform associated with a specific longitudinal displacement is the drop in output power (around 15 dBm) seen at a particular wavelength over the 1.51–1.60 μm wavelength range. This drop corresponds to a plane located behind the focal plane at this wavelength. The shift over this wavelength range follows a
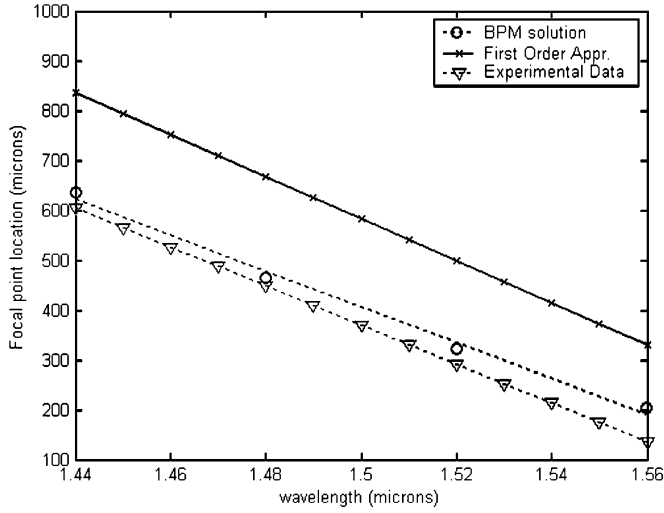
Fig. 6. FD-BPM, experimental measurements, and first-order results for focal point location as a function of wavelength.
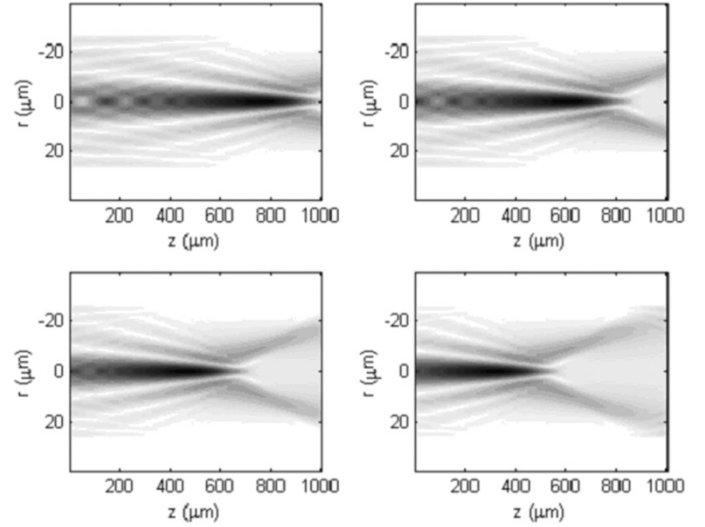

Fig. 7. Simulated field distribution, using field formulation in (18), out of the MMF facet for four different wavelengths demonstrating wavelength dependence of focal position.

linear relation whose derivative with respect to wavelength can be expressed as

$$\frac{d(z_{\text{out,exp}})}{d\lambda}\bigg|_{\lambda=1.55\ \mu\text{m}} = -3909.7\ [\mu\text{m}^{-1}]. \qquad (29)$$

This drop in power can be explained by carefully observing the intensity distribution in Fig. 1(b) specifically at the locations $z = 3L_p$ and $10L_p$. Both locations correspond to local maxima along the MMF axis. For the first location, the light destructively interferes immediately after it condenses, while in the second location the destructive interference occurs before the light convergence. As the MMF is cleaved such slightly shorter than $3L_p$ the drop in power is the most notable feature. Fig. 4 shows the simulated field distribution in a region of 1 mm behind the MMF end facet using the modes expansion expressions in (3) and (28).

To compare these experimental results with the first-order approximation, the expression in (24) is used to calculate the location of the focal plane over this particular wavelength range

$$\frac{d(z_{\text{out}})}{d\lambda}\bigg|_{\lambda=1.55\ \mu\text{m}} = -4235.9\ [\mu\text{m}^{-1}]. \qquad (31)$$

Equations (30) and (31) demonstrate a correlation between the experimental measurements and the predicted linear relation in (26). In addition, a cylindrical symmetric FD-BPM is used to simulate the experimental setup. The power that couples back to the SMF is calculated for four different wavelengths. Fig. 6 depicts the results obtained using the FD-BPM in addition to the experimental and the first-order approximation results. The figure shows almost a constant shift of 200 μm between the first-order approximation and both the experimental and the FD-BPM results. This shift is due to the presence of error of about 3% in calculating the longitudinal propagation constant using the asymptotic assumption in comparison to the exact values. That results in inaccuracy of the value of L_p and thus the calculated z_{out}. This error is not as significant when estimating the change of the spot size at these planes over the operating range of wavelength using first-order approximations
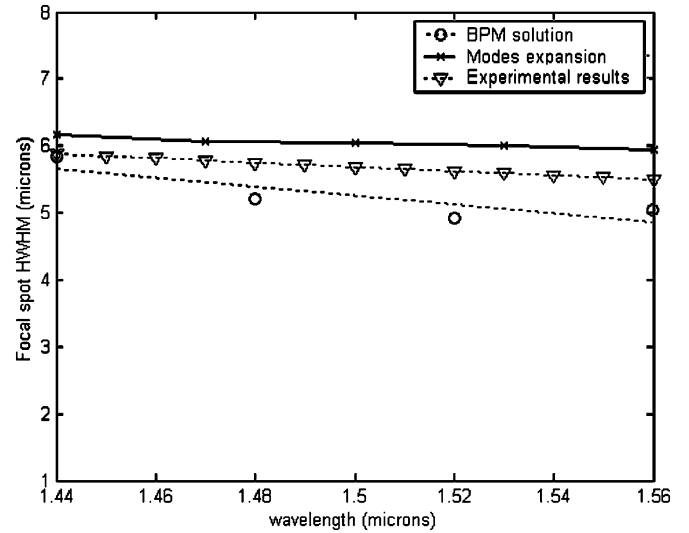

Fig. 8. Spot size (HWHM) at focal location as a function of wavelength for BPM, first-order solutions, and experimental results.

in comparison to complete FD-BPM simulations as evident in Fig. 8.

The mode series expansion expression presented by (28) is used to calculate the intensity distribution outside the MMF for four wavelengths: 1.44, 1.48, 1.52, and 1.56 μm as depicted in Fig. 7. The HWHM spot sizes at the focal planes are depicted in Fig. 8 together with the experimentally measured ones and the results from FD-BPM simulations. Looking at the curves in Fig. 8, it is apparent that the spot size slightly decreases as the wavelength is increased. An interesting property of this device is the size of the beam at the focus location associated with a particular wavelength. Simulations have shown that $>90\%$ of the input power is focused to these focus locations for a particular wavelength. To enhance the idea of the actual size of a beam at a focus location, the experimentally measured beam is depicted in Fig. 9, overlaid on the actual size of the MMF end facet.
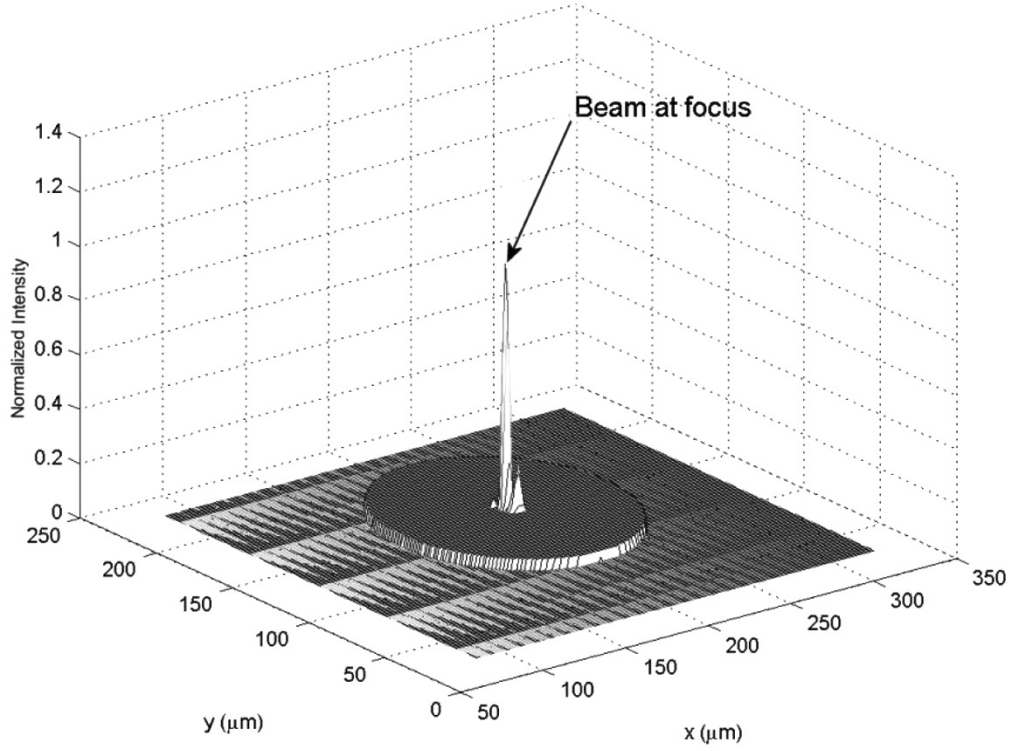
Fig. 9. Depiction of exiting beam at focus location overlaid on actual size of MMF end facet.

$$D_v = J_0^2\left(\left(2v - \frac{1}{2}\right)\frac{\pi}{2}\right) + J_1^2\left(\left(2v - \frac{1}{2}\right)\frac{\pi}{2}\right) + \left(\frac{K_1^2\left(\sqrt{V^2 - \left(\left(2v - \frac{1}{2}\right)\frac{\pi}{2}\right)^2}\right)}{K_0^2\left(\sqrt{V^2 - \left(\left(2v - \frac{1}{2}\right)\frac{\pi}{2}\right)^2}\right)} - 1\right) J_0^2\left(\left(2v - \frac{1}{2}\right)\frac{\pi}{2}\right)$$

$$D_v = J_1^2\left(\left(2v - \frac{1}{2}\right)\frac{\pi}{2}\right) + \frac{J_0^2\left(\left(2v - \frac{1}{2}\right)\frac{\pi}{2}\right)K_1^2\left(\sqrt{V^2 - \left(\left(2v - \frac{1}{2}\right)\frac{\pi}{2}\right)^2}\right)}{K_0^2\left(\sqrt{V^2 - \left(\left(2v - \frac{1}{2}\right)\frac{\pi}{2}\right)^2}\right)}$$

$$D_v' = \frac{\partial D_v}{\partial v} = 2\pi J_1\left(\left(2v - \frac{1}{2}\right)\frac{\pi}{2}\right)J_1'\left(\left(2v - \frac{1}{2}\right)\frac{\pi}{2}\right)$$

$$+ \frac{2\pi J_0\left(\left(2v - \frac{1}{2}\right)\frac{\pi}{2}\right)J_0'\left(\left(2v - \frac{1}{2}\right)\frac{\pi}{2}\right)K_1^2\left(\sqrt{V^2 - \left(\left(2v - \frac{1}{2}\right)\frac{\pi}{2}\right)^2}\right)}{K_0^2\left(\sqrt{V^2 - \left(\left(2v - \frac{1}{2}\right)\frac{\pi}{2}\right)^2}\right)\sqrt{V^2 - \left(\left(2v - \frac{1}{2}\right)\frac{\pi}{2}\right)^2}}$$

$$- \frac{2\pi J_0^2\left(\left(2v - \frac{1}{2}\right)\frac{\pi}{2}\right)K_1\left(\sqrt{V^2 - \left(\left(2v - \frac{1}{2}\right)\frac{\pi}{2}\right)^2}\right)K_1'\left(\sqrt{V^2 - \left(\left(2v - \frac{1}{2}\right)\frac{\pi}{2}\right)^2}\right)}{K_0^2\left(\sqrt{V^2 - \left(\left(2v - \frac{1}{2}\right)\frac{\pi}{2}\right)^2}\right)\sqrt{V^2 - \left(\left(2v - \frac{1}{2}\right)\frac{\pi}{2}\right)^2}}$$

$$+ \frac{2\pi J_0^2\left(\left(2v - \frac{1}{2}\right)\frac{\pi}{2}\right)K_1^2\left(\sqrt{V^2 - \left(\left(2v - \frac{1}{2}\right)\frac{\pi}{2}\right)^2}\right)K_0'\left(\sqrt{V^2 - \left(\left(2v - \frac{1}{2}\right)\frac{\pi}{2}\right)^2}\right)}{K_0^3\left(\sqrt{V^2 - \left(\left(2v - \frac{1}{2}\right)\frac{\pi}{2}\right)^2}\right)\sqrt{V^2 - \left(\left(2v - \frac{1}{2}\right)\frac{\pi}{2}\right)^2}}. \tag{A2}$$

$$\frac{\partial \eta_v}{\partial v} = \frac{2\pi\left(\left(2v - \frac{1}{2}\right)\frac{\pi}{2}\right)\left(\frac{\omega}{a}\right)^2\exp\left[-\frac{1}{2}\left(\frac{\omega^2}{a}\right)\left(\left(2v - \frac{1}{2}\right)\frac{\pi}{2}\right)^2\right]D_v - \left(\frac{\omega}{a}\right)^2\exp\left[-\frac{1}{2}\left(\frac{\omega^2}{a}\right)\left(\left(2v - \frac{1}{2}\right)\frac{\pi}{2}\right)^2\right]D_v'}{D_v^2}$$

$$= 0. \tag{A3}$$

II. CONCLUSION

We have theoretically and experimentally investigated a wavelength tunable condensing lens element based on the MMI effect. This new concept consists of a MMF fusion spliced on the end of a SMF linked to a tunable laser source. The device used to experimentally verify theoretical predictions was fabricated on an individual basis. With careful refinement of the connectorization process, it is feasible to repeatedly fabricate devices that behave the same with the same MMF splice length (± 60 μm). By using a first-order approximation and FDBPM simulation of the system, we were able to predict the relationship of the change in the focal plane in front of the end facet of the MMF with wavelength. In addition, we were able to theoretically predict the associated spot size for a given wavelength at its specific longitudinal focal location. In both cases of the relationship between change in focal plane location and associated spot size with wavelength, we were able to correlate the predicted theoretical behavior with experimentally observed results. This concept has the potential for application in near-field scanning and compact sensor systems.

APPENDIX

Using the formulation for the coupling efficiency depicted in (11), the mode number associated with peak coupling efficiency is determined by taking the derivative with respect to the mode number and equating it to zero as follows:

$$\frac{\partial \eta_v}{\partial v} = 0. \tag{A1}$$

Defining the parameters Dv and its respective derivative with respect to v, Dv': (see (A2) at the bottom of the previous page) The derivative of the coupling efficiency with respect to the mode number can thus be expressed in terms of Dv, the mode number, spot size of the input field, and the radius of the MMF core. (See (A3) at the bottom of the previous page.)

REFERENCES

[1] L. B. Soldano and E. C. M. Pennings, "Optical multi-mode interference devices based on self-imaging: Principles and applications," *J. Lightwave Technol.*, vol. 13, Apr. 1995.

[2] J. E. Zucker, K. L. Jones, T. H. Chiu, and K. Brown-Goebeler, "Strained quantum wells for polarization independent electro-optic waveguide switches," *J. Lightwave Technol.*, vol. 10, pp. 1926–1930, 1992.

[3] M. Bachmann, M. K. Smit, L. B. Solano, P. A. Besse, E. Gini, and H. Melchior, "Polarization-Insensitive low-voltage optical waveguide switch using InGaAsP/InP four port Mach–Zehnder interferometer," in *Proc. Conf. Optical Fiber Commun. (OFC)*, San Jose, CA, 1993, pp. 32–33.

[4] A. G. Mignani, A. Mencaglia, M. Brenci, and A. Scheggi, "Radially gradient-index lenses: Applications to fiber optics sensors," in *Diffractive Optics and Optical Microsystems*. New York: Martellucci and Chester, Plenum, 1997.

[5] E. G. Johnson, J. Stack, T. J. Suleski, C. Koehler, and W. Delaney, "Fabrication of micro optics on coreless fiber segments," *Appl. Opt.*, vol. 42, no. 5, Feb. 2003.

[6] R. Olshansky, "Mode coupling effects in graded-index optical fibers," *Appl. Opt.*, vol. 14, no. 4, 1975.

[7] K. Okamoto, *Fundamentals of Optical Waveguides*, P. L. Kelley, I. P. Kaminow, and G. P. Agrawal, Eds. New York: Academic, 2000, pp. 60–64.

[8] D. Marcuse, *BSTJ*, pp. 703–718, 1977.

[9] A. Mehta, W. Mohammed, and E. Johnson, "Multimode interference based fiber optic displacement sensor," *IEEE Photon. Technol. Lett.*, Aug. 2003.

[10] K. Kawano and T. Kitoh, *Introduction to Optical Waveguide Analysis*: Wiley, 2001, pp. 41–47.

[11] D. Marcuse, *Theory of Dielectric Optical Waveguide*: Academic press Inc., 1991.

[12] ——, "Mode conversion in optical fibers with monotonically increasing core radius," *J. Lightwave Technol.*, vol. 5, Jan. 1987.

Waleed S. Mohammed, photograph and biography not available at the time of publication.

Alok Mehta, photograph and biography not available at the time of publication.

Eric G. Johnson, photograph and biography not available at the time of publication.